Contents lists available at ScienceDirect

# Applied Catalysis A, General

journal homepage: www.elsevier.com/locate/apcata





# Experimental and computational study of the catalytic activity of Pd and PdCu nanoparticle catalysts and clusters supported on reduced graphene oxide and graphene acid for the suzuki cross-coupling reaction

Turbasu Sengupta <sup>a</sup>, Michael Moody <sup>b</sup>, Mrinmoy Das <sup>b</sup>, Arthur C. Reber <sup>a,\*</sup>, S.N. Khanna <sup>a</sup>, M. Samy El-Shall <sup>b,\*</sup>

#### ARTICLE INFO

# Keywords: Pd nanoparticles PdCu bimetallic nanoparticles Reduced graphene oxide support Graphene acid support Suzuki cross-coupling reaction Density functional theory

#### ABSTRACT

The catalytic activity of Pd and PdCu nanoparticle catalysts and clusters supported on reduced graphene oxide (RGO) and graphene acid (GA) toward the Suzuki cross-coupling reaction between bromobenzene and phenylboronic acid is investigated experimentally and computationally. The experimental results indicate that the bimetallic PdCu nanoparticle catalysts supported on RGO or GA outperform the supported Pd catalysts and that the PdCu/RGO catalyst exhibits superior activity, reaching a full conversion to the biphenyl product in only 15 min under ambient conditions. The experimental results show that both the Pd and PdCu catalysts have higher activities when supported on RGO than when supported on GA. The computational results using density functional theory show that the RGO provides relatively better support for the C-C coupling reaction than GA. Investigations based on the charge analysis have further revealed that the RGO is a better charge donor and acceptor than GA, facilitating both the reaction's oxidative addition and reductive elimination steps by reducing the respective barrier heights. Doping a Cu atom near the Pd reaction site is shown to enhance this effect further. The relative reactivity trends of RGO- and GA-supported Pd and PdCu clusters obtained from the DFT calculations show exact agreement with the experimental results.

## 1. Introduction

Palladium-catalyzed C-C coupling reactions are widely used in producing fine chemicals and pharmaceuticals [1–4]. The Suzuki (or the Suzuki-Miyaura) cross-coupling reaction involves the coupling of an organoboron compound with an organic halide in the presence of a Pd catalyst and base and is one of the most common reactions used to facilitate C-C bond formation. The reaction is typically performed under homogenous conditions, utilizing ligands to enhance activity and selectivity [1–4]. However, the process leads to residual metal that contaminates the reaction product. This is particularly a significant issue in pharmaceutical applications since palladium compounds can be highly toxic. Therefore, the development of supported catalysts that enhance the performance and reduce/eliminate leaching and sintering could be a major development, as it would reduce the need for post-treatment and allow for the recycling of the palladium metal. Several carbon materials are utilized for metal nanoparticle support, and

the interaction between the metal catalysts can vary depending on the support material [5–8].

A variety of graphene-based materials have been utilized for mobilizing Pd nanoparticles for cross-coupling reactions, including graphene oxide, reduced and partially reduced graphene oxides, and chemically modified graphene oxides [5–14]. Graphene is a two-dimensional material consisting of carbon atoms arranged in a hexagonal structure forming the one-atom-thick basal plane [15]. The carbon atoms contain three sp<sup>2</sup> hybridized orbitals forming sigma bonds and one p orbital likely forming pi bonds, which allow electrons to move along the graphitic plane, making graphene conductive. Graphene oxide (GO) is the oxidized form of graphene, which contain oxygenated groups on the plane, including hydroxyl, epoxy, and carboxyl groups, with the carboxyl groups residing mainly on the edges of the graphene sheets [14–16]. The presence of oxygenated groups forms defects. Pure graphene possesses conducting properties; while GO is semiconducting, the fully oxidized GO is insulating [17]. The defects sites in GO can serve as

E-mail addresses: acreber@vcu.edu (A.C. Reber), mselshal@vcu.edu (M.S. El-Shall).

<sup>&</sup>lt;sup>a</sup> Department of Physics, Virginia Commonwealth University, Richmond, VA 23284–2006, USA

b Department of Chemistry, Virginia Commonwealth University, Richmond, VA 23284–2006, USA

<sup>\*</sup> Corresponding authors.

nucleation sites for the formation and anchoring of metal nanoparticles, making GO an attractive candidate for heterogeneous catalysis [5,6, 10–14,18]. Recent studies in our group have indicated that the Pd nanocatalysts and clusters supported on reduced GO can have turnover frequencies several times higher than those of ligated clusters [5,6,10, 14].

Graphene acid (GA) is a novel graphene derivative, which contains a distribution of carboxyl groups across a graphitic plane and is synthesized by the controlled acid hydrolysis of cyanographene (G-CN) [19]. GA holds applications in nanoparticle-supported catalysis, sensing, and batteries [20–22]. It is unique in that it allows for controllable synthesis of functionalized (-COOH) groups across the graphene plane, made from the acid hydrolysis of cyanographene (G-CN). In contrast, GO synthesis is limited to less selective functionalization of oxygen groups due to its inert nature [19,23,24]. The addition of controllable synthesis of carboxylic groups across a graphitic plane is desirable because (-COOH) can facilitate unique chemistries [25–27].

In homogeneous cross-coupling catalysis, Pd is often used in the form of ligated Pd complexes which rely on the in-situ reduction of Pd (II) to Pd (0) to initiate the catalytic cycle via oxidative addition of the aryl halide reactant partner [1–4]. In heterogeneous catalysis using supported Pd nanoparticles, electronic modifications of Pd by alloying with a second metal can result in bimetallic nanoparticles with superior catalytic properties compared to their monometallic counterparts because of the ability of base metals to donate charge to the Pd centers [28]. It is expected that increasing the electron density on Pd in bimetallic alloys can lower the activation energy of the oxidative addition step of the Suzuki reactions [8]. Furthermore, alloying Pd with base metals may not only enhance the catalytic activity of the bimetallic catalysts but also make them more cost-effective because the Pd content is significantly reduced.

Here, we report a comparison of the catalytic activity of GO and GAsupported mono and bimetallic (Pd and PdCu) catalysts for the Suzuki cross-coupling reaction. Our investigations included both experimental work and detailed theoretical analysis. The experimental work investigated the catalytic activity of Pd and PdCu nanoparticle catalysts prepared by reducing Pd<sup>2+</sup> and Pd<sup>2+</sup>/Cu<sup>2+</sup> ions on the surface of the support (GO or GA) using H2 gas under high temperatures [28]. The experimental results indicate that the bimetallic PdCu catalysts supported on RGO/GA outperform the supported Pd catalysts and that the PdCu/RGO catalyst shows the best results. The purpose of the theoretical investigations is to provide insight into the experimental findings by carrying out first-principles calculations of the reaction on a variety of supports. The novelty of the joint experimental and theoretical results reported here is highlighted by developing the highly active bimetallic PdCu/RGO and PdCu/GA catalysts for room temperature Suzuki cross-coupling reactions and identifying the microscopic mechanism underlying the high catalytic activity. The high level DFT calculations reported here establish the unique ability of the PdCu/RGO system (catalyst and support) to donate and accept charges to lower the barriers for the oxidative addition and reductive elimination steps of the Suzuki cross-coupling reaction. This finding illustrates the exciting opportunities presented by the PdCu/RGO catalyst system for a variety of carbon-carbon bond forming reactions.

# 2. Methods

#### 2.1. Experimental details

# 2.1.1. Synthesis of graphene oxide (GO)

In the experiments, GO was prepared by the oxidation of high-purity graphite powder (99.999%, 200 mesh, Alfa Aesar) according to the method of Hummers and Offeman [29]. 115 mL of  $\rm H_2SO_4$  was chilled to 0 °C in an ice bath with stirring and 2.5 g of crushed NaNO<sub>3</sub> was added. After 20 min, 5 g of graphite powder was added, followed by the slow addition of 15 g of KMnO<sub>4</sub>. After 20 min, the ice bath was removed, and

the mixture was maintained at 32–38  $^{\circ}$ C for 3 h with vigorous stirring. Afterwards, 230 mL of warm DI water was added, and the temperature of 80  $^{\circ}$ C was maintained for 30 min as the solution turned brown. 700 mL of DI water was added, followed by 8 mL of 30%  $H_2O_2$  and the solution color turned to light gold. The synthesized GO was washed with 5 l of hot DI water and dried over three days at 60  $^{\circ}$ C.

#### 2.1.2. Synthesis of graphene acid (GA)

Graphene acid was synthesized via a slightly modified procedure previously reported, in which cyanographene (G-CN) is synthesized first and then G-CN groups are hydrolyzed to G-COOH groups resulting in GA [19]. 960 mg of fluorinated graphite was placed in a round bottom flask with the addition 120 mL of DMF. The mixture was sonicated for 4 h under a nitrogen atmosphere. Then, 6.4 g of NaCN was added to the suspension under 500 rpm stirring, a condenser was placed on the flask. and the reaction mixture was heated to 130  $^{\circ}\text{C}$  for 24 h. Once cooled to room temperature, 120 mL of acetone was added. The G-CN mixture was washed with the following solvents 2x each: DMF, methylene chloride, acetone, ethanol, DI water, DI water with a pH = 4 (nitric acid). The freshly washed G-CN was added to a round bottom flask in 160 mL DI water. 40 mL concentrated HNO<sub>3</sub> was added slowly under 350 rpm stirring. A condenser was attached to the round bottom flask, and the reaction was heated to 100 °C for 24 h. The GA mixture was washed three times with DI water and dried overnight at 70  $^{\circ}$ C.

#### 2.1.3. Synthesis of Pd and Pd-Cu catalysts by H2 reduction

50 mg of the support (GA or GO) was added to a beaker with 50 mL DI water and dispersed under sonication, then stirring.  $Pd(NO_3)_2$  solution was added to achieve 5 wt% initial loading. The suspension was stirred overnight and placed in the oven at 80 °C until the water was completely evaporated and the solid dried. The material was then placed in a tube furnace and heated to 200 °C for 2 h under a flow of 10 mol%  $H_2$  ( $H_2$ -He mixture) at a 30 cm3/min flow rate. The bimetallic Pd-Cu catalysts were prepared in the same methods described above with the addition of adding  $Cu(NO_3)_2$ .6  $H_2O$  solution to achieve an initial loading of 5 wt% Pd and 5 wt% Cu.

# $2.1.4. \ \textit{Procedure for room temperature Suzuki cross-coupling reactions}$

The prepared catalysts were tested towards the Suzuki coupling reaction of bromobenzene and phenylboronic acid. First, the desired amount of catalyst (0.3 mol% Pd) was charged in a screw cap vial and dispersed in 4 mL of a 1:1  $\rm H_2O\textsc{-}EtOH$  solution. 0.32 mmol of bromobenzene and 47 mg (0.38 mmol) phenylboronic acid were added to the solution under stirring. 133 mg  $\rm K_2CO_3$  (0.96 mmol) was added, and the reaction proceeded at room temperature with intermittent sampling. The samples were extracted using centrifugation and acetic acid. Gas chromatography flame ionization detector (GC-FID) was utilized to determine the ratio of bromobenzene to biphenyl product and determine the % conversion.

# 2.1.5. Characterization techniques

Powder X-ray diffraction patterns were measured using the PAN-alytical MPD X'Pert PRO diffractometer with voltage 45 kV and current 40 mA via the Ni-filtered Cu  $k\alpha_1$  radiation with a scan speed of  $2.5^\circ$   $2\theta/$  min. FTIR spectra were collected with a Thermo Scientific Nicolet iS50 FT-IR using KBr pellets. X-ray photoelectron spectroscopy (XPS) spectra of the samples were obtained using the ThermoFisher Scientific ESCA-LAB 250 with a microfocused monochromated AlK $\alpha$  X-ray source (15 kV) and a double-focusing full  $180^\circ$  spherical sector electron analyzer. TEM images were obtained using the Jeol JEM-1230 Transmission Electron Microscope with the Gatan Orius SC1000 side mount CCD camera at 120 kV. The palladium contents (wt%) of the supported catalysts were measured using the Varian Vista-MPX Inductively Coupled Plasma Optical Emission Spectrometer (ICP-OES) with an Ar $^+$  ion plasma gas equipped with a charged-couple detector (CCD) for simultaneous detection. The reaction products were analyzed using an Agilent

A 6890 N GC equipped with an HP-5MS column and a flame ionization detector used to separate and quantify the conversion of reactants into products.

#### 2.2. Computational details

The calculations of the cluster model systems are performed by the density functional theory (DFT) formalism as implemented in the Amsterdam density functional (ADF) software [30]. In all the ADF calculations, the GGA (Generalized gradient approximation) functional by Perdew-Burke-Ernzerhof (PBE) is utilized [31]. The Slater-type valance double zeta  $(\zeta)$  basis set (DZ) and the large frozen core are used for all the elements. To account for the relativistic effect, the scalar relativistic zeroth-order regular approximation (ZORA) correction is included in all the calculations [32]. All the optimizations are carried out by the hessian-based quasi-Newton approach without any symmetry constraints using the delocalized coordinates [33,34]. During optimizations, several different spin multiplicities, and various configurations are checked, and only the lowest energy structure is considered for the subsequent calculations. The analytical frequency calculation is also performed, and it is ensured that all the normal modes of the energetical minima structures are real and positive [35,36]. On the other hand, the transition states are first-order saddle points with only one imaginary frequency of appropriate magnitude. The binding energies of the Pd<sub>13</sub> cluster on the GO and GA support are calculated as,

$$\Delta E_b = E_c^{opt} + E_{\text{sup}}^{opt} - E_{cmplx}^{opt} \tag{1}$$

Here, the  $E_c^{opt}$  and  $E_{sup}^{opt}$  are the energies of the optimized Pd<sub>13</sub> cluster and the model support, respectively, and  $E_{cmplx}^{opt}$  is the energy of the overall complex. Hirshfeld charge calculations are also performed in ADF at the same theoretical level [37].

# 3. Results and discussion

# 3.1. Experimental results

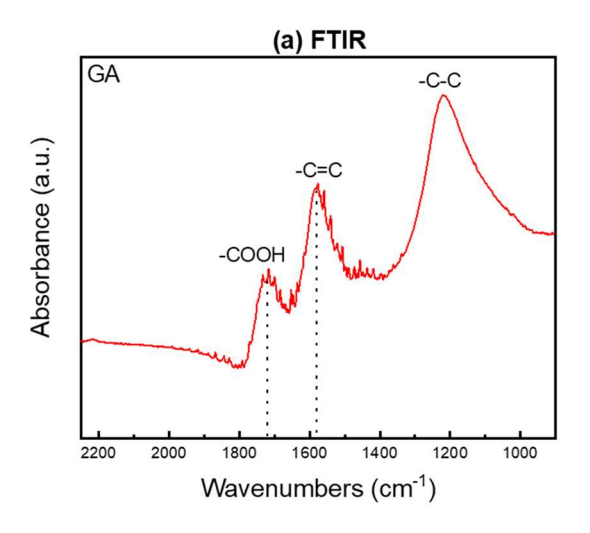
The successful synthesis GA is demonstrated clearly by the FT-IR spectrum displayed in Fig. 1(a). The spectrum shows a well-defined band at  $1723~{\rm cm}^{-1}$  corresponding to the carboxylic groups in addition to stronger bands at  $1578~{\rm cm}^{-1}$  and  $1220~{\rm cm}^{-1}$  corresponding to the C=C and C-C groups, respectively of the graphene skeleton of GA. Also, the spectrum shows no evidence for the C=N band at  $2200~{\rm cm}^{-1}$ , indicating the complete hydrolysis of cyanographene to form GA. The

overall spectrum is in excellent agreement with the FT-IR spectrum reported for GA [19].

The Raman spectra of GO and GA (displayed in Fig. 1(b)) show strong and broad G- and D-bands at 1602 cm<sup>-1</sup> and 1318 cm<sup>-1</sup> respectively. In both GO and GA spectra, the G-band is significantly broad and blue-shifted with respect to graphene (G-band  $\sim$ 1575 cm<sup>-1</sup>), which can be attributed to the presence of isolated C=C bonds that resonate at higher frequencies than the G-band of graphene [5,38]. The intensity ratio of the D-band to the G-band is usually used as a measure of the quality of the graphitic structures and the extent of structural defects and disorder since, for highly ordered graphene; this ratio approaches zero [38]. As shown in Fig. 1(b), both the GO and GA supports exhibit strong and very broad D-bands with high D/G ratios of 1.1 and 1.2, respectively, suggesting the presence of significant structural disorder and defects. These defects are expected to play an important role in enhancing the catalytic activity of the supported metallic and bimetallic nanocatalysts. The similarity of the D/G ratio of GO (1.1) and GA (1.2) strongly suggests that the two catalyst supports have comparable defect densities and degrees of disorder.

Figs. 2 and 3 display TEM images of the Pd and PdCu nanoparticle catalysts supported on the GO and GA nanosheets, respectively. In both cases, the nanoparticles appear to be well-dispersed on the surface of the support with no evidence of significant agglomeration. The size distributions of the nanoparticles determined from multiple TEM micrographs are shown in Figs. 2 and 3. For the Pd nanoparticle, the size distributions show average sizes of  $1.85\pm0.90$  nm and  $1.49\pm0.85$  nm for the particles supported on GO and GA, respectively. For the bimetallic PdCu nanoparticles, the average size of  $3.92\pm2.60$  nm supported on GA is notably larger than the average size supported on GO (1.74  $\pm0.95$  nm). This could be due to strong electrostatic interactions between the -COOH groups on GA and the Pd $^{2+}$  and Cu $^{2+}$  ions which could result in increasing the concentrations of the adsorbed ions and enhancing the growth rates of the deposited nanoparticles.

Fig. 4 displays the XPS spectra of the Pd-3d electron in the Pd/GO, PdCu/GO, Pd/GA and PdCu/GA catalysts. The electron binding energies of 335.5 and 340.8 eV corresponding to the  $3d_{5/2}$  and  $3d_{3/2}$  of metallic palladium, respectively, are observed at higher energy values by 0.3–0.5 eV in the catalysts suggesting electron transfer from palladium to the supports GO and GA. The data show that the Pd(0)% increases from 27%–31% in the Pd-Cu/GA and Pd/GA to 47%–58% in the PdCu/GO and Pd/GO catalysts, respectively. One possibility for decreasing the % of Pd(0) in the catalysts supported on GA could be the formation of strongly bound complexes between the Pd<sup>2+</sup> ions and the -COOH groups of GA, which would decrease the reduction efficiency of



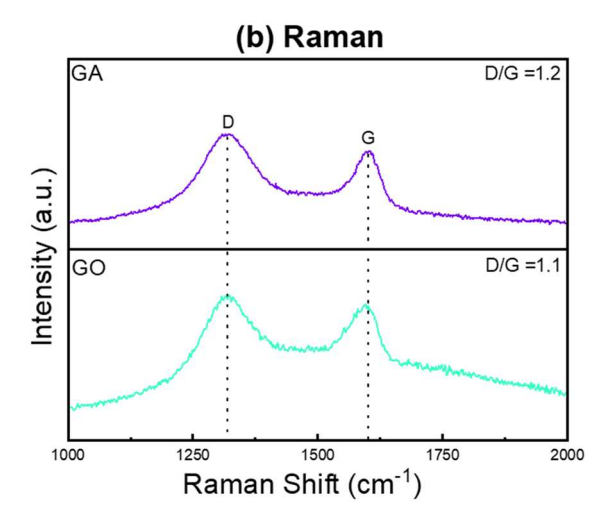


Fig. 1. (a) FT-IR spectrum of GA prepared by the hydrolysis of cyanographene. (b) Raman spectra of GA and GO show the G and D bands at 1602 cm<sup>-1</sup> and 1318 cm<sup>-1</sup>, respectively.

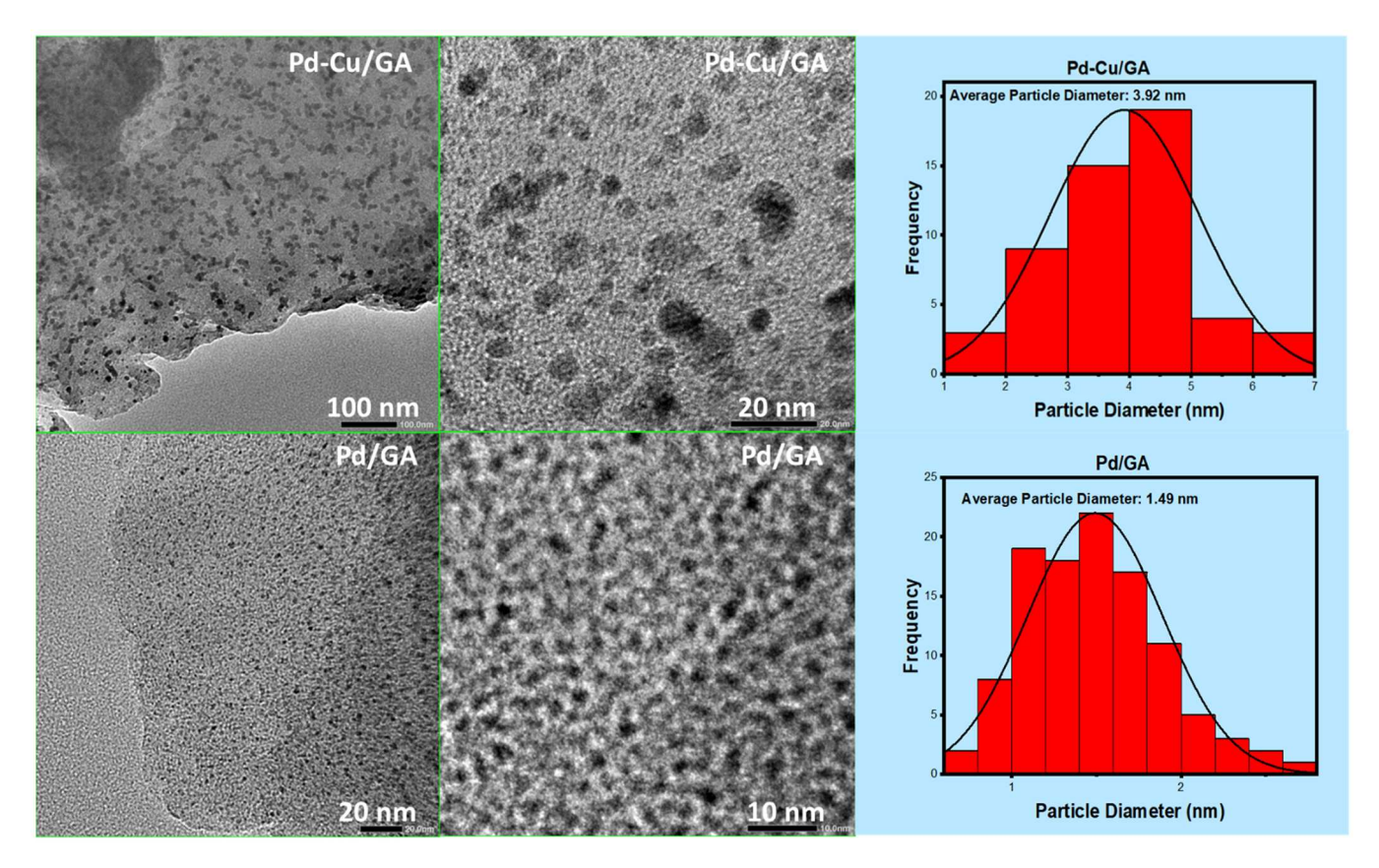


Fig. 2. TEM images and particle size distributions of the Pd and PdCu nanoparticles supported on GO nanosheets.

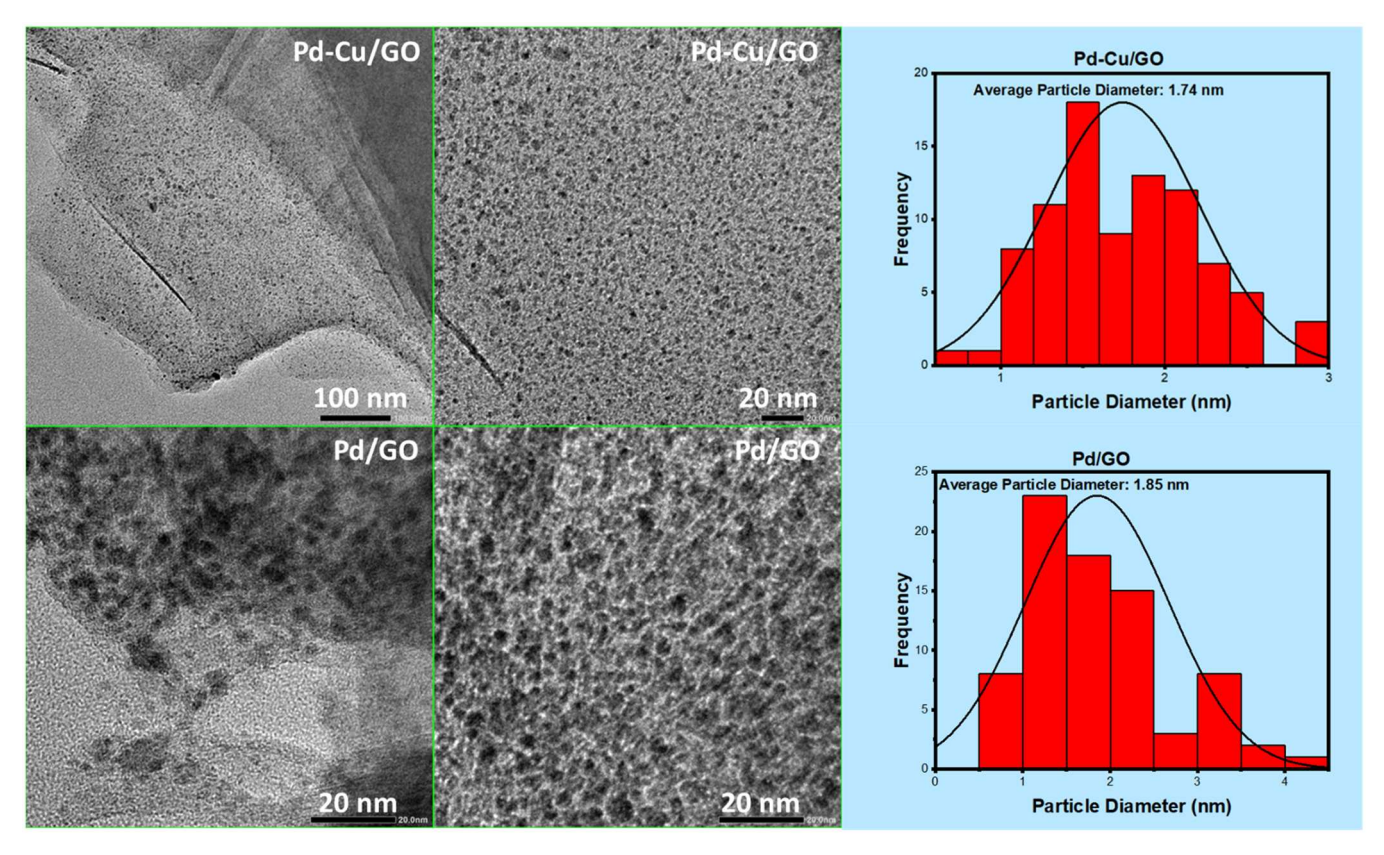


Fig. 3. TEM images and particle size distributions of the Pd and PdCu nanoparticles supported on GA nanosheets.

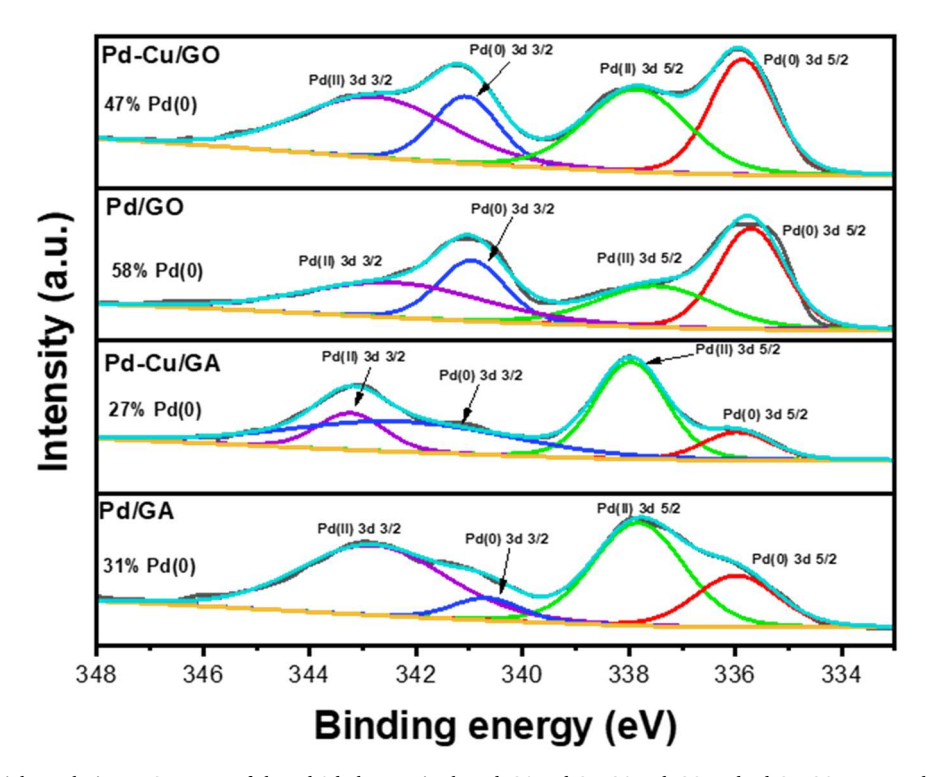


Fig. 4. High-resolution XPS spectra of the Pd-3d electron in the Pd/GA, Pd-Cu/GA, Pd/GO and Pd-Cu/GO supported catalysts.

the  $Pd^{2+}$  ions by the  $H_2$  gas.

It is known that in the palladium-catalyzed Suzuki cross-coupling reaction, the oxidation state of palladium cycles between Pd(II) in the oxidative addition of a halide-bearing aryl group and Pd(0) in the reductive elimination step [39], and that Pd(0) is required to initiate the oxidative addition step [40,41]. It is also established that a higher ratio of Pd(0) in the supported catalysts would usually result in higher catalytic activity [42]. Based on this consideration and the XPS results shown in Fig. 4, one would expect the Pd and PdCu catalysts supported on GO to have higher activity than the corresponding catalysts supported on GA. This point will be further checked and discussed in analyzing the catalytic activity results below.

The catalytic activity of the prepared Pd and PdCu catalysts was investigated using the Suzuki cross coupling reaction of bromobenzene (0.32 mmol) and phenylboronic acid (0.38 mmol) with a 0.3 mol% Pd catalyst in a mixture of  $\rm H_2O:C_2H_5OH$  (1:1) at room temperature (r.t.) according to Scheme 1.

The biphenyl product was further characterized by NMR. Examples of the  $^1\mathrm{H}$  and  $^{13}\mathrm{C}$  NMR spectra of the product synthesized using the Pd/GO catalyst are shown in Fig. S1(A) (Supplementary Data). Similar spectra were obtained for the products synthesized using the Pd/GA, PdCu/GO and PdCu/GA. The  $^1\mathrm{H}$  NMR spectrum of the biphenyl product shows one doublet and two triplets at  $\sim$  7.3–7.6 ppm. The doublet at  $\sim$ 7.6 ppm corresponds to the protons at the ortho position, the triplets at  $\sim$ 7.45 and  $\sim$ 7.36 ppm are assigned to the protons at the meta and para positions, respectively of the biphenyl. The  $^{13}\mathrm{C}$  NMR spectrum shows a peak at  $\sim$ 141.4 ppm assigned to the alpha carbon, and the three peaks at  $\sim$ 129,  $\sim$ 127.4, and  $\sim$ 127.3 ppm are assigned to the carbons at the meta, para, and ortho positions, respectively of the biphenyl. Both the  $^1\mathrm{H}$  and

Scheme 1. na.

<sup>13</sup>C NMR spectra of the biphenyl are similar to the NMR spectra of commercial biphenyl sample shown in Fig. S1(B) (Supplementary Data).

Fig. 5 illustrates the % conversion of the room temperature reaction in Scheme 1 for the Pd and PdCu catalysts supported on GO and GA. Among all catalysts, PdCu/GO exhibits superior activity reaching a bromobenzene conversion of 78% after five minutes and a full conversion in only 15 min under ambient conditions. The second-best catalyst is other bimetallic PdCu catalyst supported on GA which reaches full conversion after nearly 50 min. On the other hand, the Pd/GO and Pd/GA catalysts reach 97% conversion after nearly 60 min, although the Pd/GO catalyst achieves higher conversions than the Pd/GA catalyst at

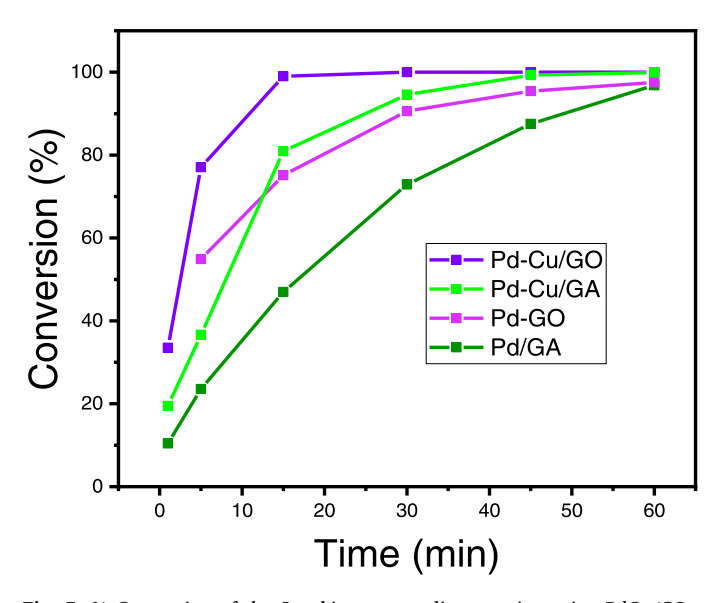


Fig. 5. % Conversion of the Suzuki cross-coupling reaction using PdCu/GO, PdCu/GA, Pd/GO and Pd/GA supported catalysts. Reaction conditions: 0.32 mmol bromobenzene, 0.38 mmol phenylboronic acid, 1 mmol  $K_2CO_3$ , and stirring speed of 450 rpm at room temperature with the Pd mol% of 0.30.

shorter reaction times. These results are significant since they demonstrate, for the first time, that the Suzuki reaction can be carried out at room temperature yielding 100% of the biphenyl product within 15 and 50 min using the bimetallic PdCu catalyst supported on GO and GA, respectively.

The superior catalytic activity of the PdCu/GO and PdCu/GA bimetallic catalysts can be explained by the electronic properties and the expected synergistic effects of the Pd and Cu metals involved in the bimetallic catalysts. According to the XPS studies, Cu in the CuPd alloy helps maintain Pd in the unoxidized state (Pd<sup>0</sup>) [28]. It is worth noting that DFT calculations of the bimetallic catalysts suggest the presence of an enhanced electronic structure factor upon metal doping which increases electron density on Pd and hence facilitates the oxidative addition of the aryl halide, which is the rate-limiting step in the Suzuki cross-coupling reaction [43,44]. This point will be addressed in detail in the next section describing the computational results of this work.

The results in Fig. 5 also show that both the Pd and PdCu catalysts have higher activities when supported on GO than when supported on GA. This is probably due to the higher Pd(0)% of the catalysts supported on GO (47%–58%), as shown in Fig. 4. The bimetallic enhancement effect appears to be significant since the PdCu/GO catalyst with a 47% Pd(0) is more active than the Pd/GO catalyst which has the highest Pd (0)% (58%). The same trend is observed on the catalysts supported on GA where the bimetallic catalyst PdCu/GA with the lowest Pd(0)% (27%) is more active than the Pd/GA catalyst, which has a higher Pd (0)% (31%). Detailed explanations of the observed activity trends will be provided by the theoretical work in the next section.

# 3.2. Computational results

To gain insight into the experimental observations, we first performed DFT simulations on both GO and GA supported Pd nanoclusters. The reaction barriers are strongly affected by the interaction of the clusters with the graphene support, as previous studies have found that

embedding the clusters within vacancies in the graphene support resulted in a dramatic decrease in the activation energy [6]. The embedding of the clusters on the surface results in improved charge transfer between the cluster and support, leading to lower activation energies. The functional groups on the support may also affect the charge transfer, so we investigated the effect of changing the functionalization of the graphene support on the reaction barriers. For this purpose, we have first designed cluster models for both GO and GA support, as shown in Fig. 6a and b. An equal number of functional groups are considered for both surfaces. We included two epoxy (-O-) and three hydroxyl (-OH) groups for the GO. Similarly, five carboxylic acid (-COOH) groups are considered for GA. The overall stoichiometric composition for the GO model is C<sub>110</sub>H<sub>28</sub>O<sub>5</sub>, and C<sub>115</sub>H<sub>30</sub>O<sub>10</sub> for the GA system. The carbon atoms at the edges were passivated for both systems by attaching H atoms. To adsorb the Pd nanoparticle, we have created a double vacancy site (by removing two C atoms) with a diameter of ~4 Å at the centre of both GO and GA surfaces (Fig. 6). The choice of double vacancy is based on the previous investigation, where it is shown that a double vacant site on graphene is thermally more stable compared to a single vacant site and hence appears more frequently, as also seen in electron microscopy [45]. The experimental observation also shows that the distribution of vacancies (defects) in the real GO and GA support systems is similar (Fig. 1(b)). This justifies using the identical number and type of vacancies for our model calculation. Both the model supports were optimized using different spin multiplicities, and the optimized structure with the lowest energy was considered for the subsequent calculations (Table S1 in the Supplementary Data). The calculated HOMO-LUMO gap of the model GO support (0.36 eV) is slightly higher than the GA support (0.08 eV). As for the Pd nanoparticle catalyst, we have considered the icosahedral  $Pd_{13}$  since previous studies have shown that the Pd nanoparticle adopts an icosahedral shape upon adsorption on graphene-based systems [6,7,46]. The optimized geometries of Pd<sub>13</sub>@GO and Pd<sub>13</sub>@GA are shown in Fig. 6c and d, and their ground state energies and spin multiplicities are given in Table S2 of the

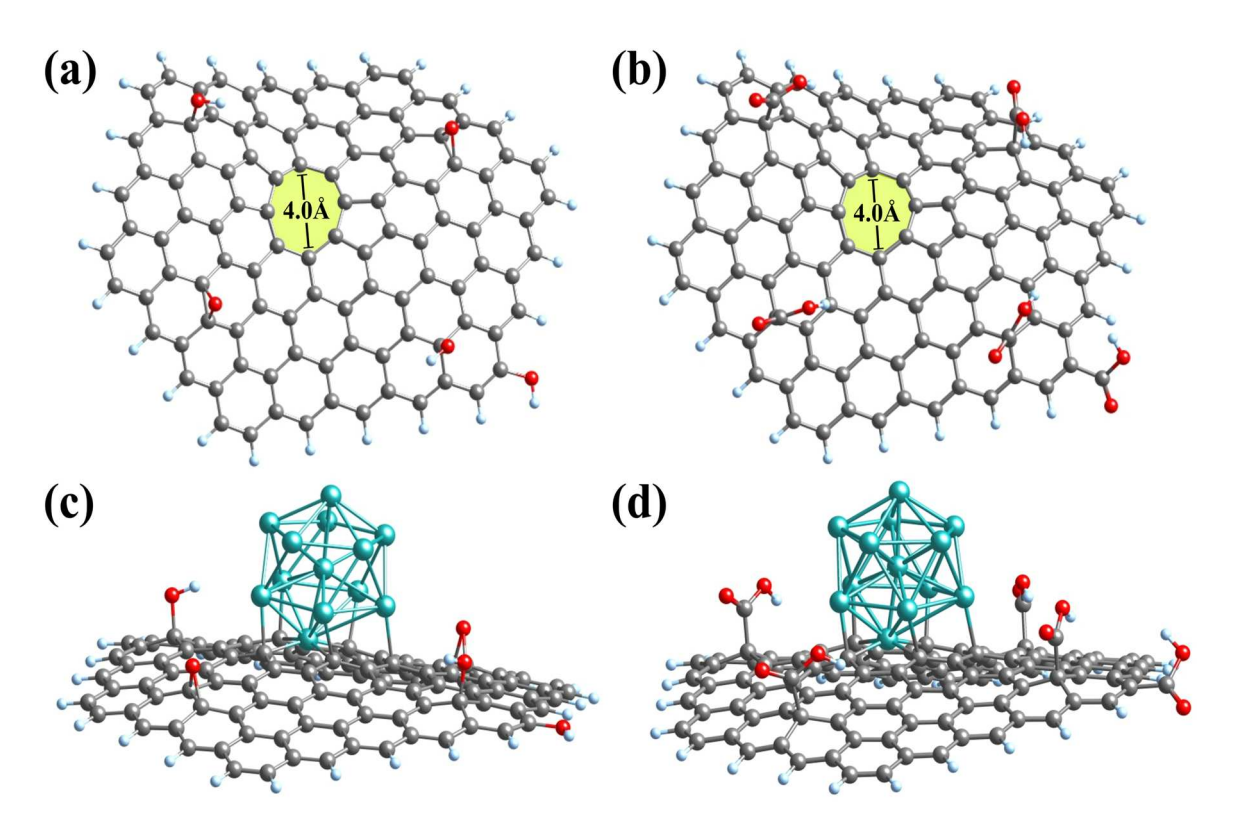


Fig. 6. Optimized structures of a) GO and b) GA cluster models with double vacancy site highlighted at the center. The ground state structures of  $Pd_{13}$  cluster adsorbed at the double vacant site of c) GO and d) GA cluster model.

Supplementary Data. The binding energies of the  $Pd_{13}$  cluster to the GO and GA support were calculated as 5.0 and 5.2 eV, respectively. The DFT calculations also reveal that the HOMO–LUMO gap of the  $Pd_{13}$ @GO and  $Pd_{13}$ @GA model systems are very close, i.e., 0.09 and 0.10 eV, respectively.

Next, we investigated the reaction pathway for the Suzuki crosscoupling reaction on the Pd<sub>13</sub>@GO and Pd<sub>13</sub>@GA model systems. For this purpose, we have considered the synthesis of biphenyl (Ph-Ph, Ph=phenyl group) via the coupling reaction between bromobenzene (Ph-Br,) and phenylboronic acid (Ph-B(OH)<sub>2</sub>) as the template reaction. In the current work, we have followed the conventional reaction pathway for the SM C-C cross-coupling reaction, as previously reported [47-49]. A general reaction schematic is included in Fig. S2 of the Supplementary Data. As known, the reaction pathway of the Suzuki coupling consists of three steps, i.e., (a) oxidative addition, (b) transmetallation, and (c) reductive elimination. Figs. 7 and 8 show the computed reaction pathway on Pd13@GO and on Pd13@GA model systems. In both cases, the optimized structures of the relevant species in the reaction pathway are arranged sequentially. During the calculations, we first determined the spin multiplicity of the lowest energy pre-reaction complex (see Table S3 of the Supplementary Data) denoted as 1 in Figs. 7 and 8 and followed the same spin multiplicity throughout the reaction pathway. The three transition states in the pathway are marked by red (Pd<sub>13</sub>@GO) or blue (Pd<sub>13</sub>@GA) color. Relative comparison between the two pathways shows that all three barrier heights in the GO pathway are lower compared to the GA pathway (Fig. 7 and Fig. 8). The difference in the barrier heights for the first two steps, i.e., oxidative addition and transmetallation, is marginal, and in the GA pathway, the barriers are only higher by 0.02 - 0.03 eV. The significant difference between both pathways is noticed in the reductive elimination step, where the GO pathway shows a 0.1 eV lower barrier compared to the GA pathway. Thus, from the computed barrier heights and especially considering the reductive elimination step, we can confirm that the Pd<sub>13</sub>@GO system is a better catalyst than the Pd<sub>13</sub>@GA system. This observation is consistent with the experimental results.

To rationalize the trend in the barrier heights of the oxidative addition and reductive elimination steps, as observed in Figs. 7 and 8, we have calculated the net Hirshfeld [37] charge transfer from the cluster@support systems to the reactant fragments for both redox steps.

It is observed that for the oxidative addition step  $(1 \rightarrow 2 \rightarrow 3 \text{ in Figs. 7 and})$ 8), the net charge transfer from the supported catalyst to bromobenzene is similar for  $Pd_{13}$ @GO (-0.26 |e|) and  $Pd_{13}$ @GA (-0.25 |e|), which is the reason for the marginal differences in the oxidative addition barrier heights for these two systems. On the contrary, the net charge transfer from the reactant fragments to the cluster@support at the reductive elimination step  $(8 \rightarrow 9 \rightarrow 10 \text{ in Figs. 7 and 8})$  is relatively higher for  $Pd_{13}@GO (-0.32 |e|)$  if compared to  $Pd_{13}@GA (-0.28 |e|)$ . This is possibly the reason for the observed lower reductive elimination barrier heights for  $Pd_{13}@GO$  (0.30 eV) compared to  $Pd_{13}@GA$  (0.40 eV). Comparing the data for both the supported system, it can be said that the graphene oxide supported Pd<sub>13</sub> cluster is a relatively better charge donor and an acceptor than Pd<sub>13</sub>@GA. This ability to act as both an effective charge donor and an acceptor was seen previously in reduced graphene with no functionalization [6]. To summarize, the Pd<sub>13</sub>@GO system is observed to be acting as a better donor (oxidative addition) and as a better acceptor (reductive elimination) compared to GA, which accounts for its relatively better catalytic performances toward the SM cross-coupling reaction.

As a final step, we explored the possibility of changing the barrier by using a mixed model cluster (Cu<sub>2</sub>Pd<sub>11</sub>) where two of the Pd atoms adjacent to the reaction (Pd) site are replaced with Cu. In a recent computational investigation, we have shown that by doping a Pd cluster with group-11 atom (e.g., Ag), it is possible to activate the nearby Pd sites toward the oxidation and reduction steps of Suzuki cross-coupling reaction resulting in reduced barriers for both steps [50]. Further analysis has revealed that the charge transfer between the dopant and the nearby Pd atoms is responsible for such alterations, and detailed explanations and analysis are given in the original publication [50]. In the current work, we have computed two similar pathways for the Zuzuki cross-coupling reaction on the Cu<sub>2</sub>Pd<sub>11</sub>@GO and Cu<sub>2</sub>Pd<sub>11</sub>@GA model systems. The reaction profiles for Cu<sub>2</sub>Pd<sub>11</sub>@GO and Cu<sub>2</sub>Pd<sub>11</sub>@GA systems are shown in Fig. 9 and Fig. 10, respectively. We have adopted the lowest energy spin state obtained for the pre-reaction complex to calculate the whole reaction pathway (Table S4, Supplementary Data).

As shown in Fig. 9,  $Cu_2Pd_{11}$ @GO shows the lowest barrier heights for the two redox steps (0.04 and 0.22 eV, respectively) compared to the rest of the systems reported in this study. Similar to the supported  $Pd_{13}$  cluster, we have performed a Hirshfeld charge transfer analysis on the

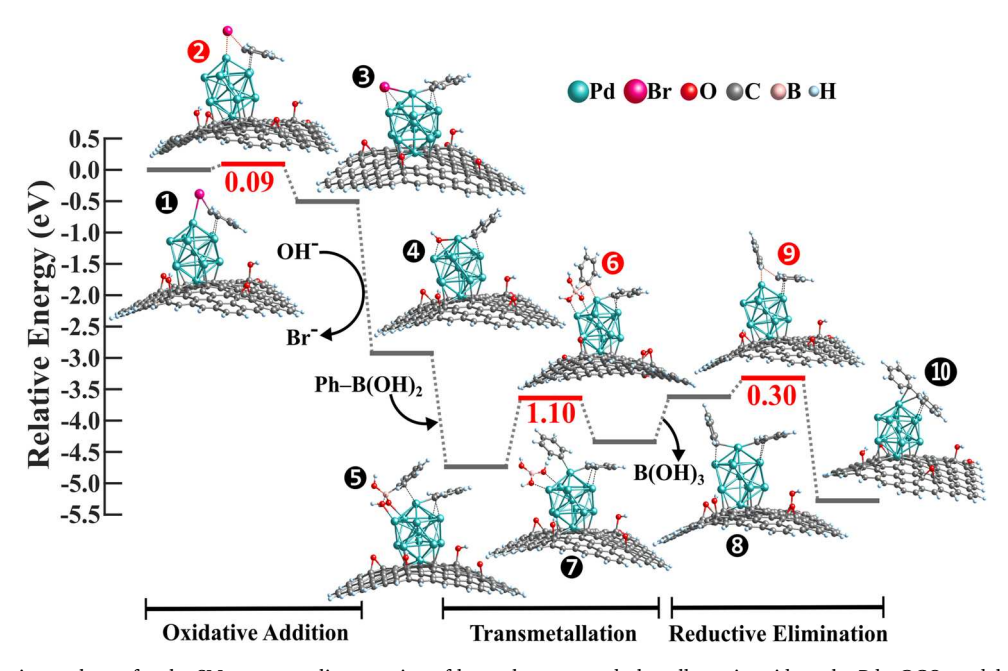


Fig. 7. Calculated reaction pathway for the SM cross-coupling reaction of bromobenzene and phenylboronic acid on the  $Pd_{13}$ @GO model system. The activation barriers of the three important steps are shown in eV. The transition states are marked by red color.

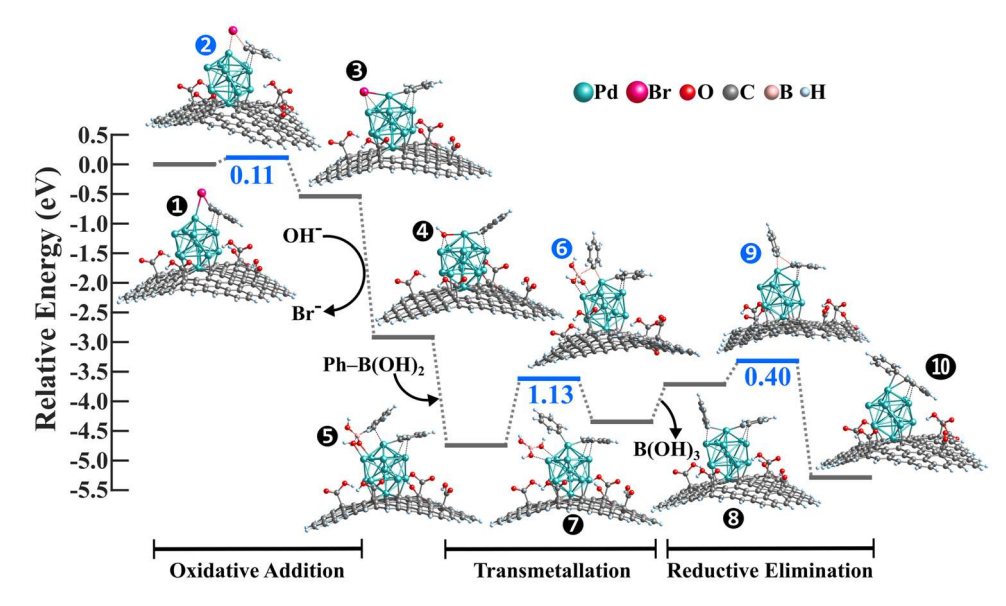


Fig. 8. Calculated reaction pathway for the SM cross-coupling reaction of bromobenzene and phenylboronic acid on the  $Pd_{13}$ @GA model system. The activation barriers of the three important steps are shown in eV. The transition states are marked by blue color.

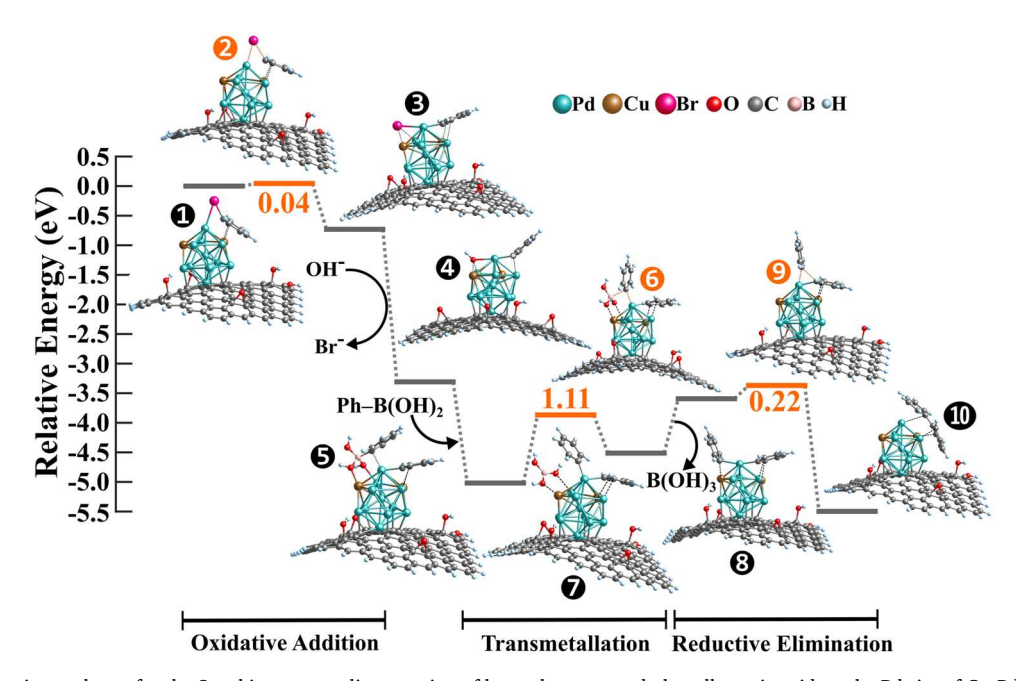


Fig. 9. Calculated reaction pathway for the Suzuki cross-coupling reaction of bromobenzene and phenylboronic acid on the Pd site of  $Cu_2Pd_{11}@GO$  model system. The activation barriers of the three important steps are shown in eV. The transition states are marked by orange color.

supported  $Cu_2Pd_{11}$  cluster systems as well [37]. Hirshfeld charge analysis shows that the  $Cu_2Pd_{11}$  cluster on both GO and GA surfaces are positively charged (+1.25 |e| on GO and +1.35 |e| on GA support). The majority of this positive charge is localized on Pd, whereas in both cases, Cu atoms show near zero accumulated charge on them. In both cases, the reaction is considered to happen on a Pd site close to the dopant (Cu) atoms. This is also because we have observed that the pre-reaction complex (shown as 1 in Figs. 9–10) is  $\sim$ 0.15 eV more stable when the bromobenzene is close to a Cu site.

Similar to the supported pristine cluster system, we noticed that the charge transfer from the supported catalyst to bromobenzene is relatively higher in the oxidative addition stage ( $1\rightarrow2\rightarrow3$  in Figs. 9–10) for Cu<sub>2</sub>Pd<sub>11</sub>@GO (-0.23 |e|) compared to Cu<sub>2</sub>Pd<sub>11</sub>@GA (-0.21 |e|) which is consistent with the calculated barrier heights. However, the net Hirshfeld charge transfer analysis for the reductive elimination step

 $(8 \rightarrow 9 \rightarrow 10$  in Figs. 9–10) shows near similar charge transfer from the phenyl fragments to the supported cluster in both cases ( $\sim -0.33$  |e|). Therefore, in this particular case, we believe that the Hirshfeld charge analysis failed to show consistent results with the observed barrier height trend, as shown in Fig. 11. Overall, from the calculated barrier heights, we can say that the inclusion of Cu dopant to the cluster enhances the catalytic effect of the supported system toward Suzuki crosscoupling, making the Cu<sub>2</sub>Pd1<sub>1</sub>@GO system the best catalyst reported in this study.

To summarize, we have observed that doping with group 11 metal atoms (e.g., Cu) enhances the catalytic potential of the cluster compared to the pristine cluster, irrespective of the type of support surface. Fig. 11 displays the barrier heights of both the redox steps for the four systems reported herewith. From the barrier heights and especially considering the reductive elimination step, one can establish a qualitative trend of

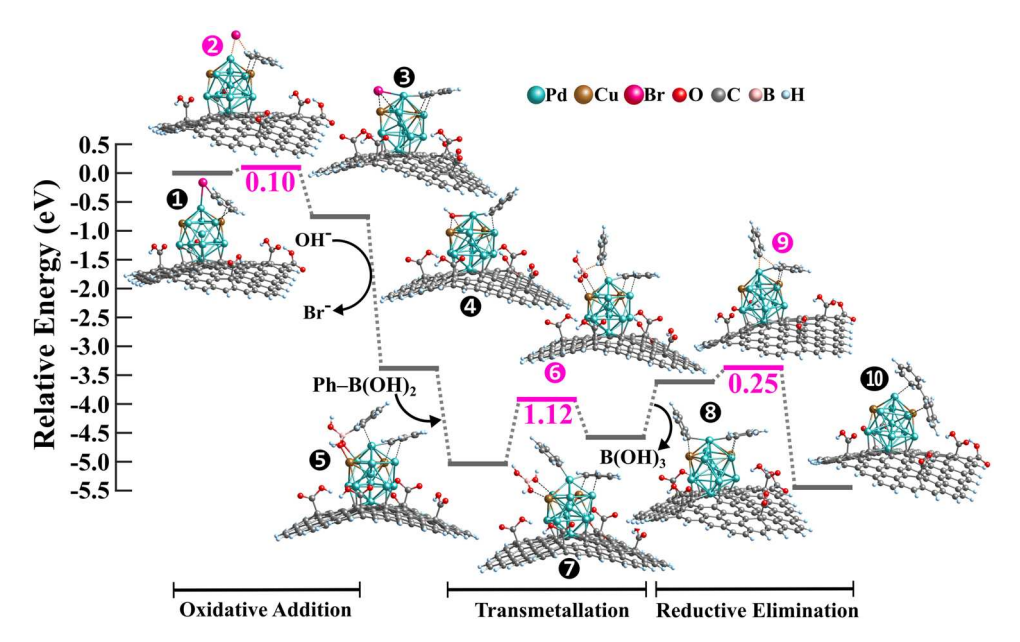


Fig. 10. Calculated reaction pathway for the Suzuki cross-coupling reaction of bromobenzene and phenylboronic acid on the Pd site of  $Cu_2Pd_{11}@GA$  model system. The activation barriers of the three important steps are shown in eV. The transition states are marked by pink color.

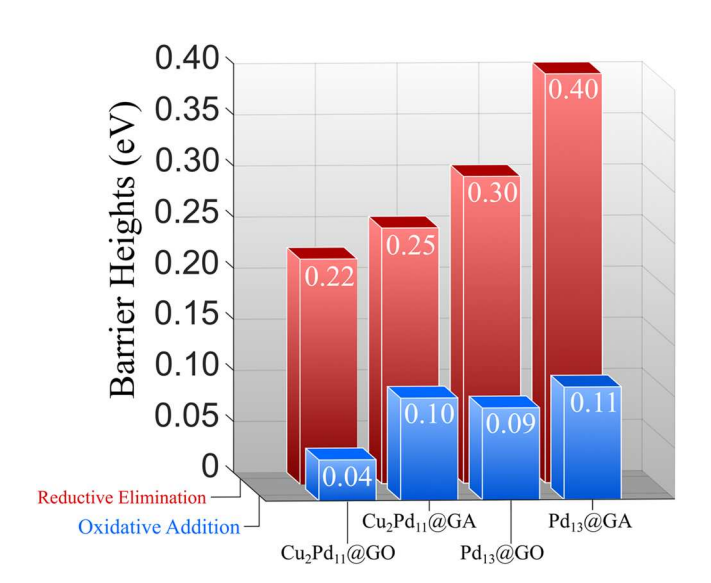


Fig. 11. Bar plot of the computed barrier heights of oxidative addition and reductive elimination steps for the four supported cluster systems.

the catalytic activity, i.e.,  $Cu_2Pd_{11}$  @GO  $> Cu_2Pd_{11}$ @GA  $> Pd_{13}$ @GO  $> Pd_{13}$ @GA, which is in exact agreement with the experimental observations.

# 4. Conclusions

The present joint experimental and theoretical studies indicate that the bimetallic PdCu catalysts supported on reduced graphene oxide (RGO) or graphene acid (GA) outperform the supported Pd catalysts toward the Suzuki cross-coupling reaction, and that both the Pd and PdCu catalysts have higher activities when supported on RGO than when supported on GA. The computational results using density functional theory demonstrate that the reaction barriers are controlled by the ability of the supported cluster to act as the charge donor and acceptor. For the pure Pd $_{13}$  cluster, the choice of support provides this flexibility, and Pd $_{13}$ @GO combination acts as a better donor (oxidative addition) and as a better acceptor (reductive elimination) compared to GA, which

accounts for its better catalytic performances toward the Suzuki cross-coupling reaction. An added ability to enhance donor/acceptor capacity is to surround the Pd sites with noble element Cu that has an unfilled 4 s shell allowing it to accept or donate charge. Indeed, Cu<sub>2</sub>Pd<sub>11</sub>@GO, which combines the effect of alloying and support, is shown to be the best performer of all the clusters considered here. The relative reactivity trends of RGO- and GA-supported Pd and PdCu clusters obtained from the DFT calculations show exact agreement with the experimental results. The present combined experimental and computational study provides a new approach to control the catalytic performance by changing the support or alloying.

# CRediT authorship contribution statement

TS conducted all the calculations. MM and MD conducted all the experimental work. ACR, SNK and MSE analyzed the results and wrote the manuscript.

# **Declaration of Competing Interest**

The authors declare that they have no known competing financial interests or personal relationships that could have appeared to influence the work reported in this paper.

# **Data Availability**

Related data are given in the <u>Supplementary Data Appendix</u>. All additional data generated or analyzed during this study are available via request to the corresponding author.

#### Acknowledgments

We thank the National Science Foundation (CHE-1900094) for the support of this work.

# **Supplementary Material**

<sup>1</sup>H and <sup>13</sup>C NMR spectra of the biphenyl product synthesized using the Pd/GO catalyst (Fig. S1), calculated energies of optimized GO and GA support at different spin multiplicities (Table S1), calculated

energies of optimized  $Pd_{13}$ @GO and  $Pd_{13}$ @GA systems at different spin multiplicities (Table S2), A general schematic of Suzuki cross-coupling reaction (Fig. S2), calculated energies of pre-reaction complex (1) of  $Pd_{13}$ @GO and  $Pd_{13}$ @GA pathway at different spin multiplicities (Table S3), and calculated energies of pre-reaction complex (1) of  $Cu_2Pd_{11}$ @GO and  $Cu_2Pd_{11}$ @GA pathway at different spin multiplicities (Table S4).

#### Appendix A. Supporting information

Supplementary data associated with this article can be found in the online version at doi:10.1016/j.apcata.2023.119448.

#### References

- [1] N. Miyaura, A. Suzuki, Chem. Rev. 95 (1995) 2457-2483.
- [2] A. Suzuki, J. Organomet, Chem 653 (2002) 83-90.
- [3] A. Balanta, C. Godard, C. Claver, Chem. Soc. Rev. 40 (2011) 4973-4985.
- [4] A. Biffis, P. Centomo, A. Del Zotto, M. Zecca, Chem. Rev. 118 (2018) 2249-2295.
- [5] A.R. Siamaki, A.E.R.S. Khder, V. Abdelsayed, M.S. El-Shall, B.F. Gupton, J. Catal. 279 (2011) 1–11.
- [6] Y. Yang, A.C. Reber, S.E. Gilliland III, C.E. Castano, B.F. Gupton, S.N. Khanna, J. Catal. 360 (2018) 20–26.
- [7] Y. Yang, C.E. Castano, B.F. Gupton, A.C. Reber, S.N. Khanna, Nanoscale 8 (2016) 19564–19572.
- [8] Y. Yang, A.C. Reber, S.E. Gilliland, C.E. Castano, B.F. Gupton, S.N. Khanna, J. Phys. Chem. C. 122 (2018) 25396–25403.
- [9] G.M. Scheuermann, L. Rumi, P. Steurer, W. Bannwarth, R. Mülhaupt, J. Am. Chem. Soc. 131 (2009) 8262–8270.
- [10] S. Moussa, A.R. Siamaki, B.F. Gupton, M.S. El-Shall, ACS Catal. 2 (2011) 145–154.
- [11] Y. Nishina, J. Miyata, R. Kawai, K. Gotoh, RSC Adv. 2 (2012) 9380-9382.
- [12] H.A. Elazab, A.R. Siamaki, S. Moussa, B.F. Gupton, M.S. El-Shall, Appl, Catal. Gen. 491 (2015) 58–69.
- [13] H.A. Elazab, S. Moussa, A.R. Siamaki, B.F. Gupton, M.S. El-Shall, Catal. Lett. 147 (2017) 1510–1522.
- [14] A.A. Ibrahim, A. Lin, M.S. Adly, M.S. El-Shall, J. Catal. 385 (2020) 194–203.
- [15] W. Yu, L. Sisi, Y. Haiyan, L. Jie, RSC Adv. 10 (2020) 15328-15345.
- [16] S. Moussa, V. Abdelsayed, M.S. El-Shall, Chem. Phys. Lett. 510 (2011) 179–184.
- [17] V. Abdelsayed, S. Moussa, H.M. Hassan, H.S. Aluri, M.M. Collinson, M.S. El-Shall, J. Phys. Chem. Lett. 1 (2010) 2804–2809.
- [18] S.O. Moussa, L.S. Panchakarla, M.Q. Ho, M.S. El-Shall, ACS Catal. 4 (2014) 535–545.
- [19] A. Bakandritsos, M. Pykal, P. Błoński, P. Jakubec, D.D. Chronopoulos, K. Poláková, V. Georgakilas, K. Cepe, O. Tomanec, V. Ranc, A.B. Bourlinos, R. Zbořil, M. Otyepka, ACS Nano 11 (2017) 2982–2991.

- [20] I. Obraztsov, A. Bakandritsos, V. Šedajová, R. Langer, P. Jakubec, G. Zoppellaro, M. Pykal, V. Presser, M. Otyepka, R. Zbořil, Adv. Energy Mater. 12 (2022) 2103010.
- [21] A. Lenarda, A. Bakandritsos, M. Bevilacqua, C. Tavagnacco, M. Melchionna, A. Naldoni, T. Steklý, M. Otyepka, R. Zbořil, P. Fornasiero, ACS Omega 4 (2019) 19944–19952.
- [22] M. Blanco, D. Mosconi, M. Otyepka, M. Medved, A. Bakandritsos, S. Agnoli, G. Granozzi, Chem. Sci. 10 (2019) 9438–9445.
- [23] S. Eigler, A. Hirsch, Angew. Chem. Int. Ed. 53 (2014) 7720-7738.
- [24] D.R. Dreyer, S. Park, C.W. Bielawski, R.S. Ruoff, Chem. Soc. Rev. 39 (2009) 228–240.
- [25] N.-F. Chiu, H.-T. Yang, Front. Bioeng. Biotechnol. 8 (2020) 234.
- [26] M.-L. Li, Y. Li, J.-B. Pan, Y.-H. Li, S. Song, S.-F. Zhu, Q.-L. Zhou, ACS Catal. 10 (2020) 10032–10039.
- [27] Y. Wang, C. Wang, Z. Ni, Y. Gu, B. Wang, Z. Guo, Z. Wang, D. Bin, J. Ma, Y. Wang, Adv. Mater. 32 (2020) 2000338.
- [28] N. Norouzi, M.K. Das, A.J. Richard, A.A. Ibrahim, H.M. El-Kaderi, M.S. El-Shall, Nanoscale 12 (2020) 19191–19202.
- [29] W.S. Hummers Jr., R.E. Offeman, J. Am. Chem. Soc. 80 (1958), 1339–1339.
- [30] G. Te Velde, F.M. Bickelhaupt, E.J. Baerends, C. Fonseca Guerra, S.J.A. van Gisbergen, J.G. Snijders, T. Ziegler, J. Comput. Chem. 22 (2001) 931–967.
- [31] J.P. Perdew, K. Burke, M. Ernzerhof, Phys. Rev. Lett. 77 (1996) 3865.
- [32] E. Van Lenthe, J.G. Snijders, E.J. Baerends, J. Chem. Phys. 105 (1996) 6505-6516.
- [33] L. Fan, T. Ziegler, J. Chem. Phys. 95 (1991) 7401–7408.
- [34] M. Swart, F. Matthias, Bickelhaupt, Int. J. Quantum Chem. 106 (2006) 2536-2544.
- [35] A. Bérces, R.M. Dickson, L. Fan, H. Jacobsen, D. Swerhone, T. Ziegler, Comput. Phys. Commun. 100 (1997) 247–262.
- [36] H. Jacobsen, A. Bérces, D.P. Swerhone, T. Ziegler, Comput. Phys. Commun. 100 (1997) 263–276.
- [37] F.L. Hirshfeld, Theor Chim, Acta 44 (1977) 129-138.
- [38] M.S. Dresselhaus, A. Jorio, M. Hofmann, G. Dresselhaus, R. Saito, Nano Lett. 10 (2010) 751–758.
- [39] A.H. Labulo, B.S. Martincigh, B. Omondi, V.O. Nyamori, J. Mater. Sci. 52 (2017) 9225–9248.
- [40] G.A. Molander, B. Biolatto, J. Org. Chem. 68 (2003) 4302-4314.
- [41] A. Mahanta, N. Hussain, M.R. Das, A.J. Thakur, U. Bora, Appl. Organomet. Chem. 31 (2017), e3679.
- [42] B.J. Reizman, Y.-M. Wang, S.L. Buchwald, K.F. Jensen, React. Chem. Eng. 1 (2016) 658–666.
- [43] T. Sperger, C.M. Le, M. Lautens, F. Schoenebeck, Chem. Sci. 8 (2017) 2914–2922.
- [44] E. Alvaro, J.F. Hartwig, J. Am. Chem. Soc. 131 (2009) 7858-7868.
- [45] F. Banhart, J. Kotakoski, A.V. Krasheninnikov, ACS Nano 5 (2011) 26-41.
- [46] E. Gracia-Espino, G. Hu, A. Shchukarev, T. Wågberg, J. Am. Chem. Soc. 136 (2014) 6626–6633.
- [47] M. Loudon, J. Parise, Organic Chemistry, Macmillan Learning, 2015.
- [48] A.J. Lennox, G.C. Lloyd-Jones, Chem. Soc. Rev. 43 (2014) 412–443.
- [49] B. Zhang, J. Song, H. Liu, J. Shi, J. Ma, H. Fan, W. Wang, P. Zhang, B. Han, Green. Chem. 16 (2014) 1198–1201.
- [50] T. Sengupta, D. Bista, S.N. Khanna, ACS Catal. 11 (2021) 11459–11468.